Research Article

A 25 kW, 25 kHz Induction Heating Power Supply for MOVPE System Using L-LC Resonant Inverter

Mangesh Borage and Sunil Tiwari

Power Supplies and Industrial Accelerator Division, Raja Ramanna Centre for Advanced Technology, Indore 452013, India

Correspondence should be addressed to Mangesh Borage; mbb@rrcat.gov.in

A topology named L-LC resonant inverter (RI) for induction heating (IH) applications takes most of the merits of the conventional series and parallel resonant schemes, while eliminating their limitations. In this paper, fundamental frequency AC analysis of L-LC RI is revisited, and a new operating point is suggested featuring enhanced current gain and near in-phase operation as compared to the conventional operating point. An approximate analysis of the circuit with square-wave voltage source is also described highlighting the effect of auxiliary inductor on the source current waveform. The analysis also leads to an optimum choice of the auxiliary inductance. The requirements of the metal organic vapour phase epitaxy (MOVPE) system in which a graphite susceptor is required to be heated to 1200°C demanding a 25 kW, 25 kHz IH power supply, the configuration of developed IH system, and experimental results are presented.

1. Introduction

The induction heating (IH) [1] is commonly used for heat treatment of metals (hardening, tempering, and annealing), heating prior to deformation (forging, swaging, upsetting, bending, and piercing), brazing and soldering, shrink fitting, coating, melting, crystal growing, cap sealing, sintering, carbon vapor deposition, epitaxial deposition, and plasma generation. IH is a noncontact method. The heat is generated only in the part, not in the surrounding area except by radiation. The location of the heating can be defined to a specified area on the metal component, thereby achieving accurate and consistent results. As heating occurs in the object itself, IH is considered more efficient than alternative methods.

An IH system comprises a basic induction power source which provides the required power output at the required power frequency, complete with matching components, an induction coil assembly, a method of material handling, and some method of cooling. Generally, full-bridge or half-bridge resonant inverters (RIs) are most commonly used as the power supplies for IH. The equivalent model of an IH coil

with work piece can be represented in simplified form by an equivalent inductance (L_{eq}) and resistance (R_{eq}) as shown in Figure 1. If the IH coil is directly fed from a supply, the ratio of apparent to real power will be large. Therefore, the IH coil is properly compensated by capacitors and additional inductors in suitable configuration so that minimum reactive power is drawn from the source. Additionally to match the load voltage-current requirements to the available source, a matching network is required. The matching is normally achieved with the help of an isolation transformer of suitable turns ratio.

Based on the connection of compensating capacitor with the IH coil, the two most commonly used RI topologies are as follows.

(1) Series resonant inverter (SRI): the compensating capacitor is placed in series with the IH coil, and it is fed by a voltage source [2–6].

(2) Parallel resonant inverter (PRI): the compensating capacitor is placed in parallel with the IH coil, and it is fed by the current source [7–11].

FIGURE 1: Equivalent circuit representation of an IH coil.

FIGURE 2: Circuit diagram of L-LC RI for IH application.

FIGURE 3: Equivalent circuit diagram of L-LC RI for analysis.

The analysis of these circuits has been performed in great details, and the comparative assessment is also reported in the literature [12, 13].

A topology named L-LC RI has been proposed for IH applications [14–21], which takes most of the merits of SRI and PRI while eliminating their limitations. It operates with input dc voltage source, thereby eliminating bulky input current smoothening inductor. It offers high current gain, which in turn reduces the current rating of the secondary winding of matching transformer and the feeder to coil.

Metal organic vapour phase epitaxy (MOVPE) [22] is a highly controlled method for the deposition of semiconductor epitaxial layers and heterostructures, which are required for the development of several optoelectronic and electronic devices. The process of MOVPE involves a vapour phase reaction between metalorganic compound and a hydride gas, which are transported to a heated (around 1200°C) graphite susceptor, resulting in a growth of the desired material. IH is one of the preferred methods for noncontact heating of the susceptor.

The paper aims to investigate the characteristics of L-LC RI for an application demanding a 25 kW, 25 kHz IH power supply to heat graphite susceptor to 1200°C in a MOVPE system for the growth of nitride semiconductors being developed at our Institute. Section 2 describes AC analysis of L-LC CN and investigates various characteristics when the converter is operated at the resonant frequency. The suggested operating point is different than the previously proposed operating point which provides enhanced current gain with smaller auxiliary inductance and results in near in-phase operation. Section 3 describes the operation of high-Q L-LC compensating network (CN) with square-wave voltage source leading to an optimum choice of the auxiliary inductor. The requirements, description, and design of the practical system are discussed in Section 4. Experimental results are presented in Section 5.

2. Analysis of L-LC CN

Figure 2 shows the L-LC RI. Input dc source V_d could be an unregulated source (obtained with single-phase or three-phase diode rectifier and filter) or could be a regulated voltage source (obtained with single-phase or three-phase diode/SCR rectifier and filter or another front-end switch-mode regulator). In the former case, regulation of the power to the work piece should be done in the RI stage using frequency variation [23, 24], fixed-frequency pulse width modulation (PWM) [25–27], or pulse density modulation (PDM) [28, 29]. In the latter case, the output control can be done by varying V_d, providing easy control of the output
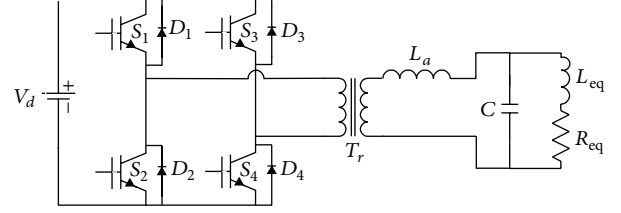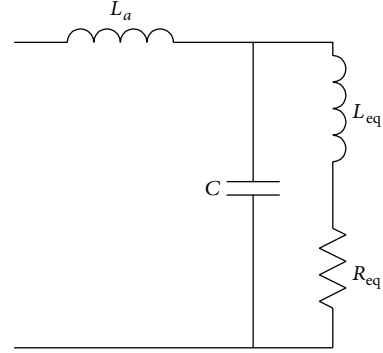
power over a wide range. However, two cascaded converters tend to reduce the overall efficiency.

The following analysis based on the fundamental frequency approximation examines the important characteristics of L-LC topology. In an equivalent circuit of L-LC CN, shown in Figure 3, input voltage source is assumed to be a sinusoidal voltage source whose rms value is equal to the rms value of the fundamental component of the square-wave excitation. Following definitions are made for the analysis.

Angular resonant frequency:

$$\omega_o = 2\pi f_o = \frac{1}{\sqrt{L_{eq}C}}. \tag{1}$$

Normalized operating frequency:

$$\omega_n = \frac{\omega}{\omega_o}, \tag{2}$$

where $\omega = 2\pi f$ is the angular operating frequency and f is the operating or switching frequency.
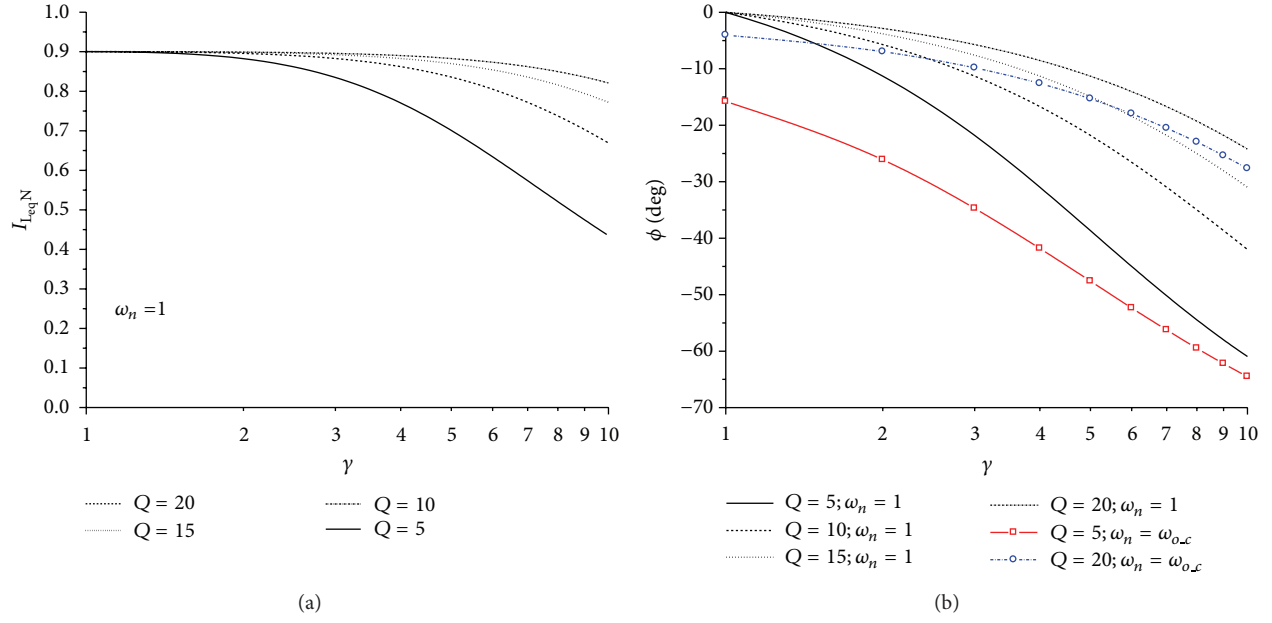
Characteristic Impedance:

$$Z_n = \sqrt{\frac{L_{eq}}{C}}. \tag{3}$$

Circuit Q:

$$Q = \frac{\omega_o L_{eq}}{R_{eq}} = \frac{Z_n}{R_{eq}}. \tag{4}$$

Inductance ratio:

$$\gamma = \frac{L_a}{L_{eq}}. \tag{5}$$

FIGURE 4: The plots of $I_{L_{eq}N}$ (a) and ϕ (b) as a function of γ for different values of Q at two operating points.

The expression for normalized current in coil and normalized source current (or the current in inductor L_a) can be, respectively, derived as

$$
\begin{aligned}
I_{L_{eq}N} &= \frac{I_{L_{eq}}}{V_d/Z_n} \\
&= \frac{2\sqrt{2}}{\pi} \frac{1}{(1/Q)\left(1 - \omega_n^2 \gamma\right) + j\left[\omega_n(1+\gamma) - \omega_n^3 \gamma\right]}, \\
I_{L_aN} &= \frac{I_{L_a}}{V_d/Z_n} \\
&= \frac{2\sqrt{2}}{\pi} \frac{\left(1 - \omega_n^2\right) + j\omega_n(1/Q)}{(1/Q)\left(1 - \omega_n^2 \gamma\right) + j\left[\omega_n(1+\gamma) - \omega_n^3 \gamma\right]}.
\end{aligned}
$$
(6)

Next, the salient characteristics of the converter operating at the proposed operating point, $\omega_n = 1$, are investigated, leading to the following observations:

(1)

$$
\left.\left|I_{L_{eq}N}\right|\right|_{\omega_n=1} = \frac{2\sqrt{2}}{\pi} \frac{Q}{\sqrt{Q^2 + (1-\gamma)^2}}.
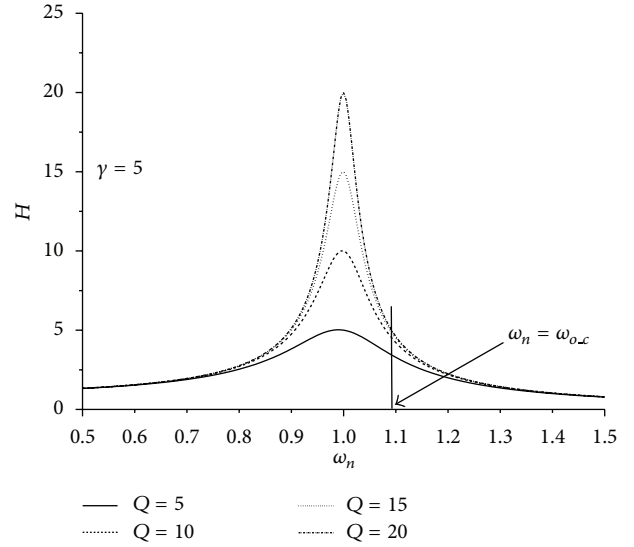$$
(7)

For $Q \gg |(1-\gamma)|$,

$$
\left.\left|I_{L_{eq}N}\right|\right|_{\omega_n=1} \approx \frac{2\sqrt{2}}{\pi},
$$
(8)

(2)

$$
\left.\left|I_{L_aN}\right|\right|_{\omega_n=1} = \frac{2\sqrt{2}}{\pi} \frac{1}{\sqrt{Q^2 + (1-\gamma)^2}},
$$
(9)

$$
\left.\phi\right|_{\omega_n=1} = \left.\angle I_{L_aN}\right|_{\omega_n=1} = -\tan^{-1}\left(\frac{\gamma-1}{Q}\right).
$$
(10)

FIGURE 5: The plots of H as a function of ω_n for $\gamma = 5$.

The source current at $\omega_n = 1$ is also seen to be inductive for all values of $\gamma > 1$, and the phase angle is function of Q and γ. If $\gamma = 1$, the source current is always in-phase with voltage.

Figure 4(a) shows the plot of $I_{L_{eq}N}$ as a function of γ for different values of Q. When the converter is operated at $\omega_n = 1$, $I_{L_{eq}N}$ is seen to be relatively insensitive to γ, particularly at high values of Q—a typical operating condition in an IH application.

Figure 4(b) shows the plot of ϕ as a function of γ. The source current lags the applied square-wave voltage $\omega_n = 1$. While this lagging current is beneficial for zero-voltage-switching (ZVS) of the semiconductor switches, it can be anticipated that a higher value of ϕ results in higher source
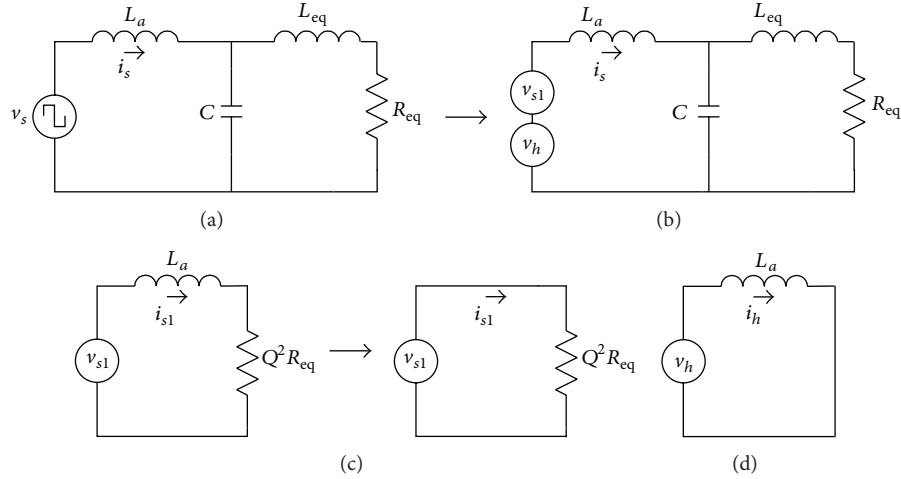
FIGURE 6: (a) Equivalent circuit for L-LC RI for analysis with v_s. (b) Equivalent circuit redrawn with v_s decomposed into v_{s1} and v_h. (c) Approximate equivalent circuit for fundamental frequency. (d) Approximate equivalent circuit for harmonics frequencies.

current causing more conduction loss in the switches. It is evident from the plots of Figure 4(b) that ϕ is small for operation at $\omega_n = 1$, particularly for operation with high Q. Therefore, the source current and conduction loss in the switches will be smaller at this operating point.

The current gain of the CN, H, is given by

$$H = \frac{I_{L_{eq}N}}{I_{L_aN}} = \frac{1}{(1 - \omega_n^2) + j\omega_n(1/Q)}, \quad (11)$$

which can further be simplified at $\omega_n = 1$ as

$$|H|_{\omega_n=1} = Q. \quad (12)$$

Figure 5 shows the plot of H as a function of ω_n for $\gamma = 5$ and different values of Q. Maximum current gain (equal to Q) is observed for operation at the proposed operating point $\omega_n = 1$.

The characteristics and design of L-LC RI for IH applications operating at $\omega_n = \omega_{o\_c} = \sqrt{(1 + \gamma)/\gamma}$ have been reported extensively in the literature [15–21]. At this operating point,

$$|H|_{\omega_n=\omega_{o\_c}} = \frac{Q\gamma}{\sqrt{Q^2 + \gamma(1 + \gamma)}}. \quad (13)$$

For $Q \gg \gamma$, $|H|_{\omega_n=\omega_{o\_c}} \approx \gamma$, which is less than theoretical maximum value given by (12) at the proposed operating point. Thus, as also shown in Figure 5, the proposed operating point of L-LC RI results in the enhanced current gain. Further, the expression for ϕ at the conventional operating point can be written as

$$\phi|_{\omega_n=\omega_{o\_c}} = \tan^{-1}\left(-\frac{\gamma}{Q}\sqrt{\frac{1+\gamma}{\gamma}}\right). \quad (14)$$

The plots of (14) as a function of γ are shown in Figure 4(b) for $Q = 5$ and $Q = 20$. It can be seen that phase angle is smaller at the proposed operating point than the conventional operating point, thereby resulting in less conduction loss in the switches.

3. Behaviour of L-LC CN with Square-Wave Voltage Source

Analysis based on the fundamental frequency approximation presented in Section 2 suggests that the converter, when operated at $\omega_n = 1$ offers highest current gain and small phase angle between source voltage and current resulting in low reactive power loading and low conduction loss in the semiconductor devices of the square-wave inverter. The analysis presented in Section 2 assumes sine wave voltage source at the input. In practice, the input voltage is a square-wave generated by operating switches S_1–S_4 in Figure 2 at 50 per cent duty cycle. In this section, the behaviour of L-LC resonant inverter for operation at $\omega_n = 1$ with square-wave voltage source examined. Equivalent circuit for L-LC RI for analysis with square-wave voltage source is shown in Figure 6(a). The source voltage v_s can be defined as

$$v_s(t) = V_d \cdot \text{sign}(\sin(\omega_o t)), \quad (15)$$

v_s can be decomposed into its fundamental component v_{s1} and harmonics v_h as

$$v_s(t) = v_{s1}(t) + v_h(t) = \frac{4V_d}{\pi}\sin(\omega_o t) + v_h(t). \quad (16)$$

From (15) and (16)

$$v_h(t) = V_d \cdot \text{sign}(\sin(\omega_o t)) - \frac{4V_d}{\pi}\sin(\omega_o t)$$

$$= V_d - \frac{4V_d}{\pi}\sin(\omega_o t) \quad \text{for } 0 \le t \le \frac{T_s}{2} \quad (17)$$

$$= -V_d - \frac{4V_d}{\pi}\sin(\omega_o t) \quad \text{for } \frac{T_s}{2} \le t \le T_s,$$

wherein T_s is the switching period. Thus, equivalent circuit of Figure 6(a) can be redrawn as Figure 6(b), wherein v_s decomposed into v_{s1} and v_h.

(a)

(b)

$\gamma = 1$ $\gamma = 5$
$\gamma = 2$ $\gamma = 7$
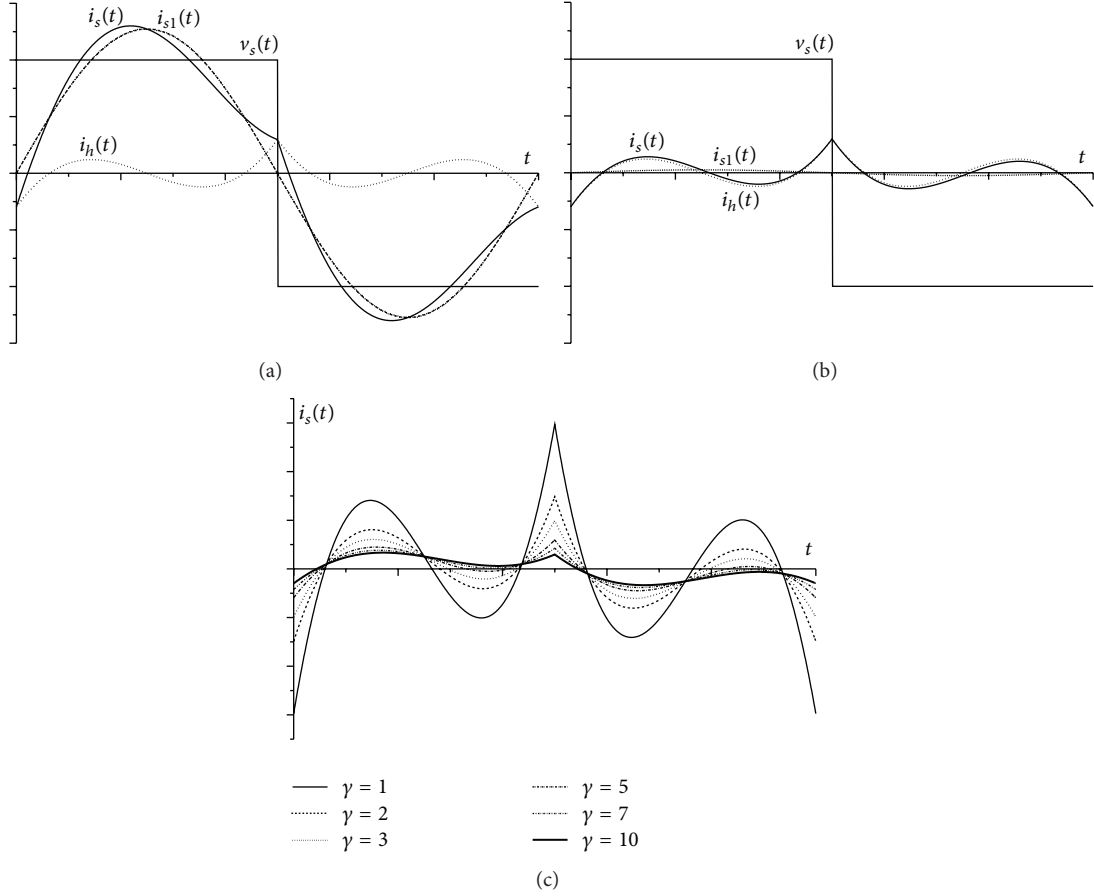$\gamma = 3$ $\gamma = 10$

(c)

FIGURE 7: Typical calculated waveforms of $v_s(t)$, $i_{s1}(t)$, $i_h(t)$, and $i_s(t)$ for low-Q ($Q = 1$; $\gamma = 1$) (a) and high-Q ($Q = 50$; $\gamma = 1$) (b) operation. The effect of γ on the waveform of $i_s(t)$ is illustrated by the calculated waveforms in (c) for $Q = 50$.

Equivalent impedance (Z_{eq}) of the L_{eq}, R_{eq}, and C resonant circuit at $\omega_n = 1$ is given by

$$\left. |Z_{eq}| \right|_{\omega_n=1} = R_{eq} Q \sqrt{1 + Q^2} \approx R_{eq} Q^2 \quad \text{for } Q \gg 1. \quad (18)$$

Further, for high-Q resonant circuit in IH applications, Z_{eq} can be approximated to be zero for all operating points other than $\omega_n = 1$. Under this assumption, equivalent circuit for Figure 6(b) can be decoupled for operation at $\omega_n = 1$ and at harmonic frequencies, as shown in Figures 6(c) and 6(d), respectively. Assuming $R_{eq} Q^2 \gg \omega_o L_a$, equivalent circuit at $\omega_n = 1$ can further be simplified as shown in Figure 6(c). With this simplification, the circuit can be analyzed for fundamental and harmonic frequencies separately to find out individual source current and then be added to find out resultant source current. An expression for i_s can be derived as

$$i_s(t) = i_{s1}(t) + i_h(t),$$

$$i_{s1}(t) = \frac{4V_d}{\pi Q^2 R_{eq}} \sin(\omega_o t),$$

$$i_h(t) = \frac{V_d}{L_a}\left(t - \frac{T_s}{4}\right) - \frac{4V_d}{\pi \omega_o L_a} \sin\left(\omega_o t - \frac{\pi}{2}\right)$$

$$\text{for } 0 \le t \le \frac{T_s}{2}$$

$$= -\frac{V_d}{L_a}\left(t - \frac{3T_s}{4}\right) - \frac{4V_d}{\pi \omega_o L_a} \sin\left(\omega_o t - \frac{\pi}{2}\right)$$

$$\text{for } \frac{T_s}{2} \le t \le T_s. \quad (19)$$

Figure 7(a) shows the calculated waveforms for the operation of the circuit under low-Q condition. It can be easily noticed that $i_{s1}(t)$, being inversely proportional to Q, is significantly larger than $i_h(t)$ for low-Q values. Therefore, resulting $i_s(t)$ is also nearly sinusoidal. Under this condition, the predictions of the ac analysis (Section 2) are reasonably accurate. However, under high-Q condition, as shown in Figure 7(b), amplitude of $i_{s1}(t)$ is much smaller than $i_h(t)$. Therefore, $i_s(t)$ is nearly the same as $i_h(t)$ and is highly nonsinusoidal. Under this condition, the predictions of Section 2 tend to be erroneous. Since the analysis of Section 2 does not account for harmonics, the actual peak and rms values of i_s calculated

by (3) are significantly more than those predicted by (9). This will result in degradation of the current gain from its value predicted by (12). However, the amplitude and rms value of $i_h(t)$ can be controlled by choosing a proper value of L_a. Figure 7(c) shows the calculated waveform of $i_s(t)$ for different values of γ when $Q = 50$. Since the rms value of $i_h(t)$ can be reduced by increasing the value of L_a, the degradation in the current gain can be corrected to some extent by choosing higher value of γ. Figure 8 shows the plots of current gain as a function of Q for different values of γ. A plot of the current gain predicted by (12) is also shown for direct comparison. The figure also shows the evolution of the current gain at the conventional operating point predicted by (13) for $\gamma = 1$ and $\gamma = 5$. It is noticed that the actual current gain at the proposed operating point is higher than that at the conventional operating point.

The physical size of an inductor depends on its value, peak current, and rms current. Since, peak and rms value of $i_s(t)$ decreases with increasing L_a, it is intuitive to expect that the physical size of L_a will first reduce as L_a increased, reach a minimum and subsequently increase with further increase in L_a. To obtain a value of L_a resulting in minimum size, the following term is defined as its normalized size index:

$$K_{L_a} = \frac{L_a I_{s,\text{pk}} I_{s,\text{rms}}}{L_{\text{eq}} I_{L_{\text{eq}},\text{pk}} I_{L_{\text{eq}},\text{rms}}}. \tag{20}$$

Figure 9 shows the plots of (20) for different values of Q. It is seen that for high-Q applications, L_a should typically be 5 times L_{eq}.

4. System Description

MOVPE is a highly controlled method for the deposition of semiconductor epitaxial layers and heterostructures, which are required for the development of several optoelectronic and electronic devices. The process of MOVPE involves a vapour phase reaction between metalorganic compound and a hydride gas, which are transported to a heated (around $1200°\text{C}$) graphite susceptor, resulting in a growth of the desired material. A power supply is required to heat graphite susceptor (50 mm diameter and 20 mm length) to $1200°\text{C}$ in a quartz reactor of 80 mm diameter.

4.1. Work Coil and Resonant Capacitor. While recommended coil design practices suggest that the coil should be as close to the susceptor and the coil length should be larger than that of the susceptor [1], physical dimensions of the susceptor and the reactor force the inner diameter of the coil to be 100 mm. Further, since a stainless steel showerhead with nozzles for flowing gases into the reactor is attached to one end of the reactor, the maximum length of the coil is also limited to 50 mm. The coil is made up of hollow copper conductor. The number of turns, conductor diameter, and its wall thickness are optimized considering various parameters like coil resistance, power loss, electrical efficiency, required cooling water flow rate, and pressure drop. The designed coil has 4 turns of hollow copper conductor with 3/8 inch OD and SWG 19 wall thickness. The coil resistance is estimated
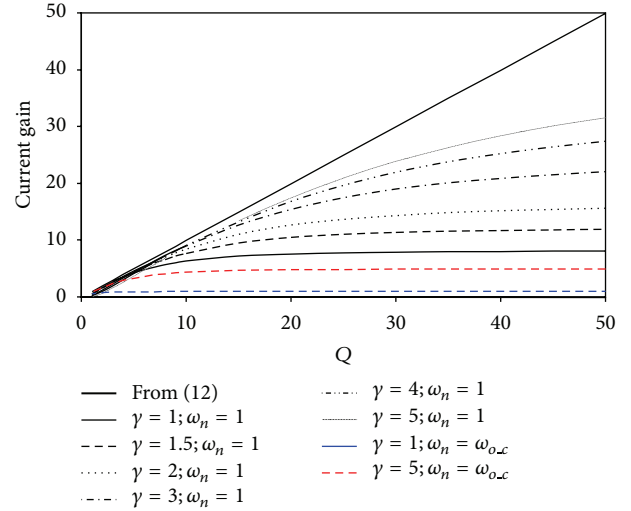

FIGURE 8: The plots of current gain as a function of Q for different values of γ at the at the proposed operating point $\omega_n = 1$ and conventional operating point $\omega_n = \omega_{o\_c}$.
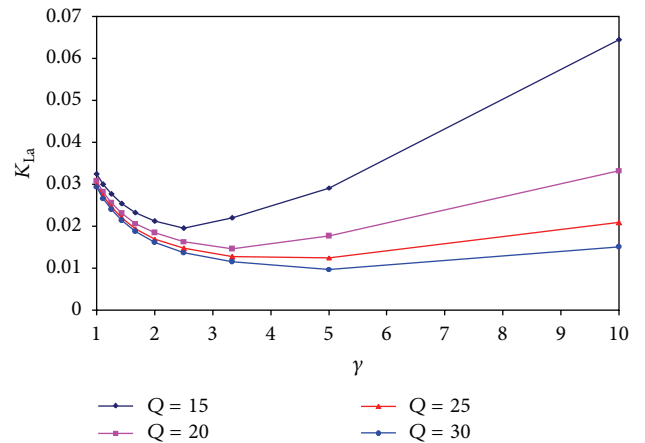

FIGURE 9: The plots of (20) showing the variation of K_{L_a} as a function of γ for different values of Q.

to be 11.3 mΩ, and coil inductance is 2.70 μH. The operating frequency of 25 kHz has been fixed to ensure uniform heating of the susceptor (the skin depth of graphite is nearly 17 mm at 25 kHz). Equivalent resistance of work piece is estimated to be 16.6 mΩ. The coil is designed to carry a maximum of 1000 A rms.

A bank of 6 conduction-cooled capacitors of 3 μF each has been used as the resonant capacitor C. These capacitors are mounted on a cold plate, which in turn is water cooled. However, only 5 capacitors are used to get the resonant frequency of 25 kHz. The capacitor bank is kept very close to the coil to reduce the circulating path.

4.2. Power Circuit. A schematic circuit diagram of the power circuit is shown in Figure 10, which can broadly be divided into three sections: front-end-three phase diode rectifier with filter, a dc-dc converter, and the L-LC RI. In addition to
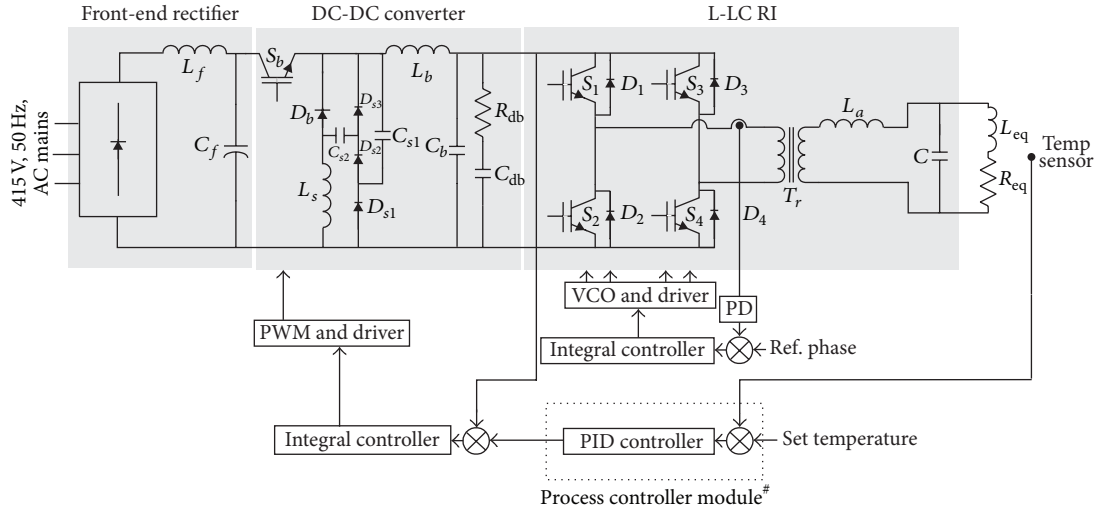
FIGURE 10: The power circuit and the control block diagram of a 25 kHz, 25 kW induction heating power supply using L-LC RI for MOVPE system. [#]The process controller, shown for the completeness, is not used in the laboratory testing of the system.

these, the actual power circuit also consists of breakers, EMI filter, and inrush-current-limiting circuit in the rectifier stage. However, these are not shown in Figure 10 for clarity.

The input to the power supply is 415 V, 50 Hz, and 3-phase ac. The values of filter inductor (L_f) and capacitor (C_f) in the input rectifier section are 2.2 mH and 3 mF, respectively, giving the cut-off frequency of 70 Hz.

It is seen in Section 2 that the L-LC RI exhibits desired behaviour only when it is operated at $\omega_n = 1$. Therefore, variation of switching frequency for output power control is not permitted. Therefore, fixed-frequency control methods such as pulse width modulation (PWM) or the quantized control methods such as pulse density modulation can be used. However, the soft-switching operation of the switches in RI stage may not be guaranteed over the entire operating range, and the quantized control methods, such as PDM, result in discrete output levels and also have limited range of output power control. If, on the other hand, input voltage to the RI stage is controlled, output power control over a wider range and operational flexibility can be ascertained. Demerits of this scheme, namely, requirement of an intermediate dc-dc converter stage and reduction of overall conversion efficiency, are sacrificed for aforementioned advantages.

A dc-dc buck converter is chosen as the intermediate dc-dc converter stage. IGBT S_b and diode D_b constitute the main switching cell. A passive loss-less snubber circuit (composed of snubber inductor L_s, capacitors C_{s1}, C_{s2}, and diodes D_{s1}, D_{s2}, and D_{s3}) is used to limit switching losses in this stage. It is worthwhile to note that apart from the careful choice of the component values, described in [30], an equal attention to several practical aspects [31], such as forward recovery of snubber diodes and stray inductances, is also important for effective snubber action. Inductor L_b, capacitors C_b, C_{bd}, and resistor R_{bd} constitute a high-frequency damped low-pass filter.

Two half-bridge IGBT modules SKM100GB123D are used to realize the H-bridge in the inverter section feeding

FIGURE 11: The photograph of the developed induction heating power supply. The graphite susceptor heated to 1200°C is shown in the inset.

square-wave voltage to the high-frequency isolation transformer. The transformer T_r having 1:1 turns ratio has been developed using 7 pairs of EE80 core with 7 turns of the primary winding and 7 turns of the secondary winding. While the primary is wound using 0.2 × 50 mm copper foil, oxygen-free high conductivity hollow copper conductor is used for water-cooled secondary winding. The results for Figure 9 suggest that the additional resonant inductor L_a should approximately be 5 times L_{eq} for high-Q operation. Therefore, in the present system, $L_a = 13.5\,\mu$H is chosen. The transformer leakage inductance is estimated to be 5 μH. The additional 8.5 μH inductance is realized by running the secondary turns around auxiliary gapped core (2 pairs of EE80), following the configuration suggested in [32].

A capacitor has been placed in series with the transformer primary (not shown in Figure 10) to prevent the transformer saturation in the event of unsymmetrical excitation. Table 1
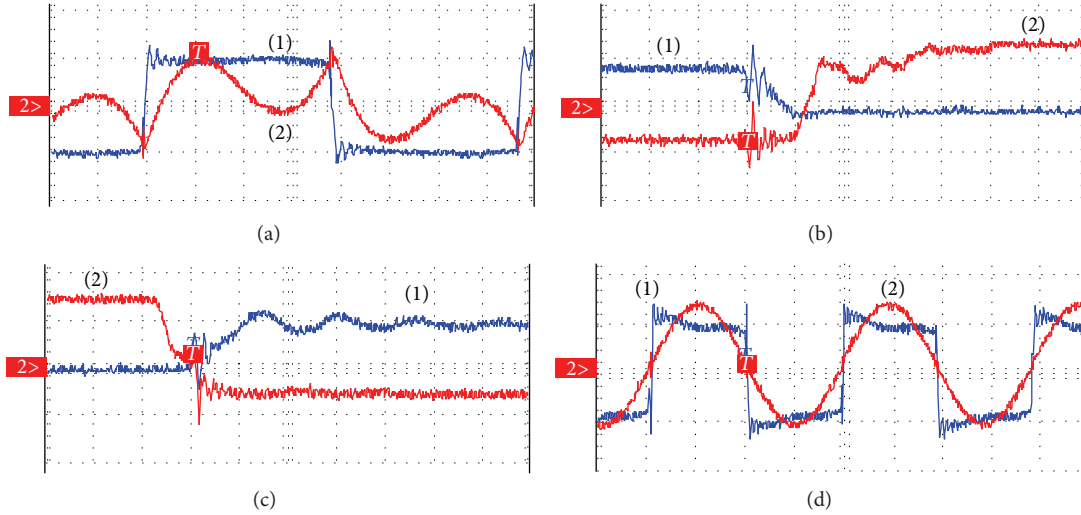
FIGURE 12: Experimental waveforms. (a) v_s (trace 1, 200 V/div) and i_s (trace 2, 25 A/div); x-scale: 5 μs/div. (b) Waveforms at turn-on: IGBT collector-to-emitter voltage (trace 1, 200 V/div) and gate-to-emitter voltage (trace 2, 10 V/div) x-scale: 500 ns/div. (c) Waveforms at turn-off: IGBT collector-to-emitter voltage (trace 1, 200 V/div) and gate-to-emitter voltage (trace 2, 10 V/div) x-scale: 500 ns/div. (d) v_s (trace 1, 200 V/div) and the voltage across the work coil (trace 2, 200 V/div) x-scale: 10 μs/div.

TABLE 1: Component values and device part numbers used in the system.

Component	Value/Part number
L_f	2.2 mH
C_f	3 mF
L_b	300 μH
C_b	30 μF
C_{bd}	150 μF
R_{bd}	2.2 Ω
L_s	5 μH
C_{s1}	0.03 μF
C_{s2}	0.33 μF
L_a	13.5 μH
C	15 μF
D_{r1}-D_{r6}	VUO 82
S_b-D_b	SKM100GAR123D
S_1-S_4 and D_1-D_4	SKM100GB123D, two modules
D_{s1}, D_{s2}, D_{s3}	DSEI 31 × 100

summarizes the values of the components and part numbers of the semiconductor devices used in the system.

4.3. Control Circuit. The input dc voltage to the square-wave inverter is controlled to regulate the susceptor temperature. The block diagram of overall control system is also shown in Figure 10. A thermocouple-type temperature sensor and process PID controller module are planned to be used for programming and controlling susceptor temperature. The output of PID module acts as the reference for the inner control loop to control the input dc voltage to the square-wave inverter by controlling the duty ratio of the buck converter. An additional phase control loop is employed to maintain

the tune-in condition of the RI stage against the slow drift of resonant frequency over varied operating conditions and time. This loop senses the phase of the inverter output current using a phase detector, PD. The output of the controller drives a voltage controlled oscillator (VCO) that adjusts the switching frequency of the inverter in such a way that the inverter output current lags the voltage slightly.

5. Results

The photograph of the developed induction heating power supply, being tested in laboratory to heat a graphite susceptor, is shown in Figure 11. The graphite susceptor heated to 1200°C in air is shown in the inset.

The inverter output voltage, v_s, (trace 1, 200 V/div) and current waveforms, i_s, (trace 2, 25 A/div) are shown in Figure 12(a). The nature of current waveform matches with the predicted waveform given in Figure 7. The waveforms of collector-to-emitter (trace 1, 200 V/div) and gate-to-emitter (trace 2, 10 V/div) voltage of an IGBT in H-bridge inverter during turn-on and turn-off transitions are shown in Figures 12(b) and 12(c), respectively, demonstrating the soft-switching. Figure 12(d) shows the waveforms of v_s (trace 1, 200 V/div) and the voltage across the work coil (trace 2, 200 V/div) showing that only fundamental component of input square-wave voltage has been passed to the work coil.
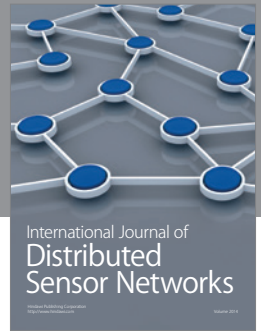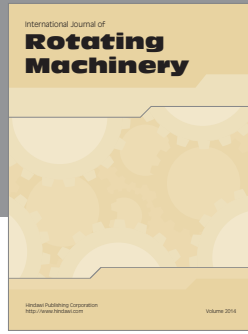
6. Conclusion

The paper reports the various issues in the development of an IH power supply for MOVPE application using L-LC RI. The fundamental frequency ac analysis of L-LC RI is revisited, and it is shown that the converter exhibits enhanced current gain and near-unity power factor operation when operated at the resonant frequency. Further analysis of

the circuit with square-wave voltage source highlights the effect of the auxiliary inductor on the source current waveform leading to the optimum choice for the value of auxiliary inductor. The requirements of MOVPE system demanding a 25 kW, 25 kHz IH power supply to heat a graphite susceptor to 1200˚C, the configuration of developed IH system, and experimental results are presented, thereby demonstrating the suitability of L-LC RI operating at its resonant frequency for this application.

References

[1] C. A. Tudbury, *Basics of Induction Heating. vol. 1*, Library of Congress Catalog Number 60-8958, 1960.

[2] I. Millán, J. M. Burdío, J. Acero, O. Lucía, and S. Llorente, "Series resonant inverter with selective harmonic operation applied to all-metal domestic induction heating," *IET Power Electronics*, vol. 4, no. 5, pp. 587–592, 2011.

[3] Ó. Lucía, J. M. Burdio, I. Millan, J. Acero, and D. Puyal, "Load-adaptive control algorithm of half-bridge series resonant inverter for domestic induction heating," *IEEE Transactions on Industrial Electronics*, vol. 56, no. 8, pp. 3106–3116, 2009.

[4] P. K. Jain, J. R. Espinoza, and S. B. Dewan, "Self-started voltage-source series-resonant converter for high-power induction heating and melting applications," *IEEE Transactions on Industry Applications*, vol. 34, no. 3, pp. 518–525, 1998.

[5] H. P. Ngoc, H. Fujita, K. Ozaki, and N. Uchida, "Phase angle control of high-frequency resonant currents in a multiple inverter system for zone-control induction heating," *IEEE Transactions on Power Electronics*, vol. 26, no. 11, pp. 3357–3366, 2011.

[6] F. Forest, E. Labouré, F. Costa, and J. Y. Gaspard, "Principle of a multi-load/single converter system for low power induction heating," *IEEE Transactions on Power Electronics*, vol. 15, no. 2, pp. 223–230, 2000.

[7] R. Bonert and J. D. Lavers, "Simple starting scheme for a parallel resonance inverter for induction heating," *IEEE Transactions on Power Electronics*, vol. 9, no. 3, pp. 281–287, 1994.

[8] E. J. Dede, V. Esteve, J. Garcia, A. E. Navarro, E. Maset, and E. Sanchis, "Analysis of losses and thermal design of high-power, high-frequency resonant current fed inverters for induction heating," in *Proceedings of the 19th International Conference on Industrial Electronics, Control and Instrumentation*, pp. 1046–1051, November 1993.

[9] E. J. Dede, J. Jordan, J. V. Gonzalez, J. Linares, V. Esteve, and E. Maset, "Conception and design of a parallel resonant converter for induction heating," in *Proceedings of the 6th Annual Applied Power Electronics Conference and Exposition (APEC '91)*, pp. 38–44, March 1991.

[10] E. J. Dede, J. Jordan, J. A. Linares et al., "On the design of medium and high power current fed inverters for induction heating," in *Proceedings of the IEEE Industry Applications Society Annual Meeting*, pp. 1047–1053, October 1991.

[11] V. Chudnovsky, B. Axelrod, and A. L. Shenkman, "An approximate analysis of a starting process of a current source parallel inverter with a high-Q induction heating load," *IEEE Transactions on Power Electronics*, vol. 12, no. 2, pp. 294–301, 1997.

[12] L. Hobson and D. W. Tebb, "Transistorized power supplies for induction heating," *International Journal of Electronics*, vol. 59, no. 5, pp. 543–552, 1985.

[13] F. P. Dawson and P. Jain, "A comparison of load commutated inverter systems for induction heating and melting applications," *IEEE Transactions on Power Electronics*, vol. 6, no. 3, pp. 430–441, 1991.

[14] G. L. Fischer and H.-C. Doht, "Inverter system for inductive tube welding utilizing resonance transformation," in *Proceedings of the 29th Institute for Advanced Study (IAS) Annual Meeting*, pp. 833–840, October 1994.

[15] J. Espi, E. Dede, A. Ferreres, and R. Garcia, "Steady-state frequency analysis of the L-LC resonant inverter for induction heating," in *Proceedings of the IEEE International Power Electronics Congress Technical Proceedings (CIEP '96)*, pp. 22–28, 1999.

[16] J. M. Espi, E. J. Dede, E. Navarro, E. Sanchis, and A. Ferreres, "Features and design of the voltage-fed L-LC resonant inverter for induction heating," in *Proceedings of the 30th Annual IEEE Power Electronics Specialists Conference (PESC '99)*, pp. 1126–1131, July 1999.

[17] J. M. Espí and E. J. Dede, "Design considerations for three element L-LC resonant inverters for induction heating," *International Journal of Electronics*, vol. 86, no. 10, pp. 1205–1216, 1999.

[18] S. Chudjuarjeen, A. Sangswang, and C. Koompai, "An improved LLC resonant inverter for induction-heating applications with asymmetrical control," *IEEE Transactions on Industrial Electronics*, vol. 58, no. 7, pp. 2915–2925, 2011.

[19] E. J. Dede, J. Gonzalez, J. A. Linares, J. Jordan, D. Ramirez, and P. Rueda, "25-kW/50-kHz generator for induction heating," *IEEE Transactions on Industrial Electronics*, vol. 38, no. 3, pp. 203–209, 1991.

[20] S. Dieckerhoff, M. J. Ryan, and R. W. De Doncker, "Design of an IGBT-based LCL-resonant inverter for high-frequency induction heating," in *Proceedings of the IEEE Industry Applications Conference and 34th IAS Annual Meeting*, pp. 2039–2045, October 1999.

[21] J. M. E. Huerta, E. J. D. G. Santamaría, R. G. Gil, and J. Castelló-Moreno, "Design of the L-LC resonant inverter for induction heating based on its equivalent SRI," *IEEE Transactions on Industrial Electronics*, vol. 54, no. 6, pp. 3178–3187, 2007.

[22] K. Nishida, S. Haneda, K. Hara, H. Munekata, and H. Kukimoto, "MOVPE of GaN using a specially designed two-flow horizontal reactor," *Journal of Crystal Growth*, vol. 170, no. 1-4, pp. 312–315, 1997.

[23] Y.-S. Kwon, S.-B. Yoo, and D.-S. Hyun, "Half-bridge series resonant inverter for induction heating applications with load-adaptive PFM control strategy," in *Proceedings of the 14th annual Applied Power Electronics Conference and Exposition (APEC '99)*, pp. 575–581, March 1999.

[24] H. W. Koertzen, J. D. Van Wyk, and J. A. Ferreira, "Comparison of swept frequency and phase shift control for forced commutated series resonant induction heating converters," in *Proceedings of the Conference Record of the IEEE Industry Applications and 30th IAS Annual Meeting*, pp. 1964–1969, October 1995.

[25] J. M. Burdío, L. A. Barragán, F. Monterde, D. Navarro, and J. Acero, "Asymmetrical voltage-cancellation control for full-bridge series resonant inverters," *IEEE Transactions on Power Electronics*, vol. 19, no. 2, pp. 461–469, 2004.

[26] L. Grajales and F. C. Lee, "Control system design and small-signal analysis of a phase-shift-controlled series-resonant inverter for induction heating," in *Proceedings of the IEEE Power Electronics Specialist Conference*, pp. 450–456, 1995.

[27] L. Grajales, J. A. Sabate, K. R. Wang, W. A. Tabisz, and F. C. Lee, "Design of a 10 kW, 500 kHz phase-shift controlled series-resonant inverter for induction heating," in *Proceedings of the 28th Annual Meeting of the IEEE Industry Applications Conference*, pp. 843–849, October 1993.

[28] N. A. Ahmed, "High-frequency soft-switching AC conversion circuit with dual-mode PWM/PDM control strategy for high-power IH applications," *IEEE Transactions on Industrial Electronics*, vol. 58, no. 4, pp. 1440–1448, 2011.

[29] V. Esteve, E. Sanchis-Kilders, J. Jordán et al., "Improving the efficiency of IGBT series-resonant inverters using pulse density modulation," *IEEE Transactions on Industrial Electronics*, vol. 58, no. 3, pp. 979–987, 2011.

[30] C.-J. Tseng and C.-L. Chen, "Passive lossless snubbers for dc/dc converters," in *Proceedings of the 13th Annual Applied Power Electronics Conference and Exposition (APEC '98)*, pp. 1049–1054, February 1998.

[31] M. Borage and S. Tiwari, "On the development of 30 kVA, 430 Hz sine wave inverter for DC accelerator application," in *Proceedings of the Indian Particle Accelerator Conference (InPAC '11)*, IUAC, New Delhi, India, February 2011.

[32] A. Kats, G. Ivensky, and S. Ben-Yaakov, "Application of integrated magnetics in resonant converters," in *Proceedings of the IEEE 12th Applied Power Electronics Conference*, pp. 925–930, February 1997.